Geophysical Journal International

Geophys. J. Int. (2012) **191,** 51–63 doi: 10.1111/j.1365-246X.2012.05620.x

Rock magnetic techniques complemented by ferromagnetic resonance spectroscopy to analyse a sediment record

Jessica Kind,[1] Ulrike J. van Raden,[2] Inés García-Rubio[3] and Andreas U. Gehring[1]

[1] *ETH Institute of Geophysics,* 8092 *Zurich, Switzerland. E-mail: jessica.kind@erdw.ethz.ch*
[2] *ETH Geological Institute,* 8092 *Zurich, Switzerland*
[3] *ETH Zurich, Laboratory of Physical Chemistry,* 8093 *Zurich, Switzerland*

Accepted 2012 July 19. Received 2012 July 17; in original form 2011 January 30

SUMMARY

Environmental magnetism uses the spatial and temporal occurrence of magnetic carriers as diagnostic tools to detect environmental changes. Concentration, composition, grain size and configuration of the carriers inferred from magnetic properties are key parameters, because they are indicative of the formation conditions of magnetic phases, and/or of processes such as diagenesis and weathering. We present a detailed ferromagnetic resonance (FMR) spectroscopy analysis in concert with routinely used rock magnetic measurements to determine these parameters in a sediment record that documents the development of Lake Soppensee (Central Switzerland) since latest Pleistocene. FMR spectroscopy monitors varying concentration of the predominant magnetite/maghemite by the spectral signal intensity, whereas the stable single domain and superparamagnetic states are determined by the signal shape at room and low temperature. Fitting and simulation of FMR spectra are successfully applied to samples with well-defined magnetite components in the sediment matrix. Clear evidence for the colonization of magnetotactic bacteria (MTB) in Lake Soppensee was possible by applying empirical spectral separation to measured FMR signals that yield two magnetite populations differing in their configuration, that is, dispersed and aligned in chains. Low temperature measurements showed that these MTB can be preserved as pure or oxidized magnetite. The FMR data set confirms and completes rock magnetic information obtained from the lacustrine sedimentary record. The advanced application of FMR spectroscopy in the presented study critically highlights the benefit of this rapid and non-destructive method for future analysis of magnetic properties in environmental studies.

Key words: Biogenic magnetic minerals; Magnetic fabrics and anisotropy; Rock and mineral magnetism.

1 INTRODUCTION

Environmental magnetism was developed about 40 yr ago. Initially based on interdisciplinary studies involving sediments from British lakes it was soon expanded to other natural (e.g. marine sediments, soils and loess) and more recently to urban systems (Thompson *et al.* 1975, 1980; Thompson & Oldfield 1986; Verosub & Roberts 1995; Evans & Heller 2003; Maher 2007). In this research field, the spatial and temporal occurrence of magnetic carriers are used as diagnostic tool to detect environmental changes that are mainly driven by climate and to a lesser extent by anthropogenic activities. The main magnetic carriers in natural systems are iron phases. Among them, iron oxide minerals, such as magnetite and hematite, that can carry remanent magnetization under ambient conditions, are of major interest. Concentration, composition, grain size and configuration of these mineral phases are key properties in environmental studies, because they are proxies for physical, chemical and biological processes during the formation of the magnetic carriers. A set of rock magnetic analyses, including the decomposition of remanence curves have been employed to determine these properties in qualitative or quantitative manner (e.g. Thompson & Oldfield 1986; Butler 1992; Egli & Lowrie 2002; Evans & Heller 2003; Egli 2004).

In the last years, first-order reversal curves (FORC) have been often used to measure coercivity spectra and interaction fields to detect MTB (Roberts *et al.* 2000; Egli *et al.* 2010; Kind *et al.* 2011). In few rock magnetic studies of natural environments, the magnetic analysis is complemented by ferromagnetic resonance (FMR) spectroscopy (e.g. Pawse *et al.* 1998; Kopp *et al.* 2006; Fischer *et al.* 2007; Maloof *et al.* 2007; Roberts *et al.* 2011). FMR spectroscopy is a well-established method in physics by which microwave absorption is measured as function of an applied magnetic field (Kittel 1948; Vonsovskii 1966). In an environmental context, FMR can be a powerful tool to detect ferrimagnetic minerals such as magnetite/maghemite that yield strong absorption spectra. The spectral parameters of the absorption are used to describe anisotropy

properties, such as magnetocrystalline and shape anisotropy fields, as well as the domain state of the minerals (Bickford 1950; Valstyn *et al.* 1962; Gehring *et al.* 2009; Mastrogiacomo *et al.* 2010). The temperature dependency of magnetocrystalline anisotropy is reflected by FMR spectra, which has been taken to distinguish between magnetite (Fe_3O_4) and its oxidized counterpart maghemite (γ-Fe_2O_3) (Bickford 1950; Fischer *et al.* 2007; Gehring *et al.* 2012). Moreover, it was argued that FMR is a powerful method to experimentally detect magnetotactic bacteria (MTB) because of their anisotropy traits (Gehring *et al.* 2011b). In MTB, single-domain magnetic particles known as magnetosomes are arranged in chains that result in pronounced interaction-induced shape anisotropy (Weiss *et al.* 2004; Kopp *et al.* 2006; Fischer *et al.* 2008; Kind *et al.* 2011). The interplay between the interaction-induced shape anisotropy and the magnetocrystalline anisotropy of magnetosome chains was shown in FMR spectral simulations based on physical grounds (Charilaou *et al.* 2011b). Furthermore, Charilaou *et al.* (2011a) simulated the anisotropy changes from cellular non-interacting superparamagnetic particles to interacting stable single domain particles during the development of magnetosome chains.

The simulation of FMR spectra obtained from natural samples is limited because the variation in composition, grain size and configuration of the magnetic carriers often generates superposition of spectral responses. For cases where the spectral superposition hampers the quantitative description of the anisotropy traits, an empirical spectral separation approach can provide qualitative information about anisotropy properties of the magnetic carriers. It is worth noting that spectra obtained from natural samples often exhibit superposition of FMR and electron spin resonance (ESR) signals. The latter originates from paramagnetic ions (e.g. Fe(III), Mn(II), V(IV), radicals) with no long-range magnetic order (e.g. Abragram & Bleaney 1970). Such paramagnetic species, structure-bound in minerals, however, have successfully been used as redox-indicator in different geological systems (e.g. Gehring *et al.* 1994).

Spectroscopic measurements are fast and provide comprehensive magnetic information. Moreover, recent progress in the analytical treatment of FMR spectra enables a more advanced extraction of quantitative or qualitative information that could be used to decipher magnetic changes in environmental systems. The purpose of this research is to demonstrate the potential of advanced FMR spectroscopic analysis for environmental magnetism using a sediment record from Lake Soppensee as example.

2 BACKGROUND

2.1 Lake Soppensee

Lake Soppensee is a small, hard water lake situated on the Central Swiss Plateau (596 m a.s.l., 8°20′00″E, 47°05′30″N). It was formed during the end of the Last Glacial stage due to the retreat of the Reuss glacier from the Swiss foreland (Schlüchter 1988). The geomorphological position and the shape of the lake suggest that the kettle was formed by dead-ice (Lotter 1989). The lake covers a surface of approximately 0.27 km^2, has a maximum depth of 27 m, and a drainage basin of 1.6 km^2. In the last decades the Soppensee has been extensively studied, and a solid database is available (e.g. sedimentological, hydrological, pollen and radio carbon data) that is beneficial to put the magnetic and spectroscopic data in an environmental context (e.g. Lotter 1989; Hajdas *et al.* 1993, 2000; Fischer 1996; Lotter 1999, 2001; Blockley *et al.* 2008; Hajdas & Michczynski 2010).

2.2 The sediment record

The sediment record is a composite of three UWITEC-piston cores that were recovered from a water depth of approximately 26 m with overlapping sequences. The record was correlated based on sedimentology and magnetic susceptibility logs and has a total length of 670 cm, covering the Holocene and the latest Pleistocene (Fig. 1). The age-depth model was developed by correlating published radiocarbon ages (Hajdas & Michczynski 2010) to our sediment cores. In addition, four plant macrofossil remains were dated (59 cm: 400 yr uncal BP; 250.95 cm: 2835 yr uncal BP; 319.80 cm: 42301 yr uncal BP; 337.05 cm: 4825 yr uncal BP; each with an error of ±40 yr). All data were calibrated (INTCAL09) and modelled using a depositional *P*-sequence model of the OxCal 4.1.7 calibration program (Ramsey 2008). Ages are reported in calibrated calendar years BP (before AD 1950). Sedimentological features permit a subdivision of the record into six units (A–F) that cover a time range of about 18 kyr cal BP. The deepest unit F (670–560 cm) is characterized by gravels and sands deposited during the last deglaciation period (older than 14 kyr cal BP). These clastic materials are overlain by light gray, glacio-lacustrine clays that mark the boundary to unit E. This unit (560–505 cm) consists of dark brownish, partly laminated sediments, mainly carbonates, silty clays and a considerable amount of organic matter. As described in Lotter (1999) and Hajdas & Michczynski (2010), unit E can be attributed to the Bølling/Allerød (14–12 kyr cal BP) and the Younger Dryas period (12–11 kyr cal BP); the Laacher See tephra (12.7 kyr cal BP) is found within this unit Hajdas & Michczynski (2010). In unit D (480–360 cm) the varved sediment consists of grayish, laminated calcareous gyttja, an alternating accumulation of organic matter and calcite that marks the beginning of the Holocene. The varved sediment exhibits a gradual change in hue from dark gray (11 kyr cal BP) to light beige (≈8 kyr cal BP) and back to dark gray (6 kyr cal BP). Unit C (360–170 cm) consists of very dark sediments with organic-rich material that have been dated to approximately 6–2 kyr cal BP (Hajdas & Michczynski 2010). Sediments from unit B (170–35 cm) with an appropriate age of about 2–0.2 kyr cal BP consist of material with whitening in colour. Unit A, the topmost part of the core (<35 cm), contains light brown sediments. Further information about the sediments from the Soppensee can be found elsewhere (e.g. Lotter 1989; Hajdas *et al.* 1993; Fischer 1996; Lotter 1999; Gruber *et al.* 2000; Hajdas *et al.* 2000; Livingstone & Hajdas 2001; Lotter 2001; Blockley *et al.* 2008; Hajdas & Michczynski 2010).

3 SAMPLES AND METHODS

A total of 400 samples covering the entire sedimentary record were taken at intervals of 2.5 cm and sealed in 12.2 cm^3 plastic cubes. The cubes were stored at 4°C to prevent drying-out and chemical alteration of the sediment.

In a first step all samples were analysed by the following rock magnetic methods. The natural remanent magnetization (NRM) was measured and subsequently demagnetized in 23 steps with maximum alternating field (AF) of 120 mT to determine the median destructive field (MDF_{NRM}) of the magnetic carriers. The MDF_{NRM} is defined as the AF value needed to reduce the intensity of the initial remanence by one-half. The measurements were performed on fresh samples using a 2G Enterprise, model 755R, 3-axis DC-SQUID magnetometer, equipped with a direct current (DC) coil for anhysteretic remanent magnetization (ARM) experiments. The following magnetic analyses were conducted on

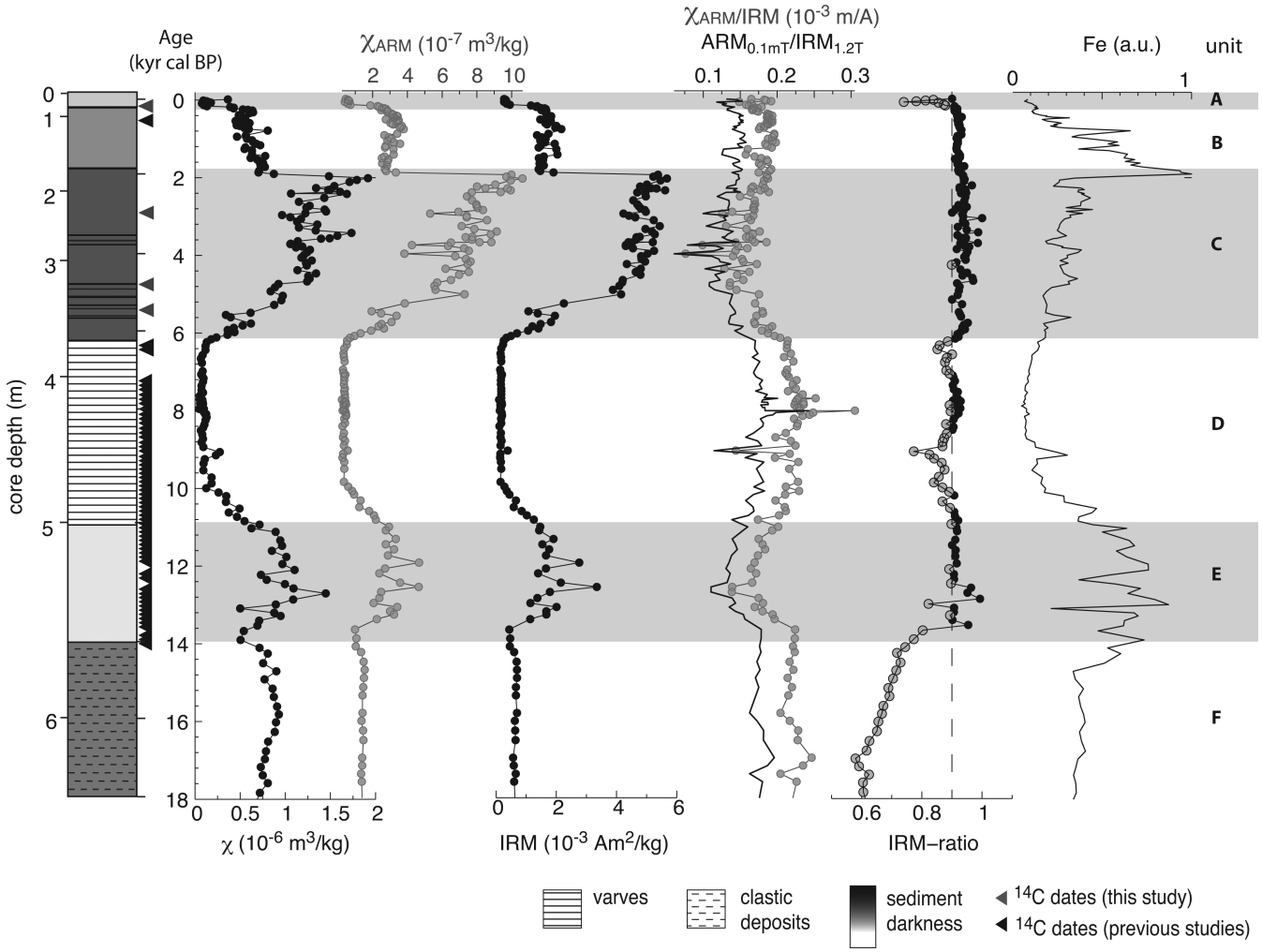

Figure 1. Stratigraphic record of Lake Soppensee with units A–F: magnetic susceptibility (χ), anhysteretic susceptibility (χ_{ARM}), isothermal remanent magnetitzation at 1.2 T ($IRM_{1.2T}$), anhysteretic over isothermal remanent magnetization (the ratio was calculated for samples that saturate below 1.2 T fields; $ARM_{0.12T}/IRM_{1.2T}$), IRM-ratio ($IRM_{120mT}/IRM_{1.2T}$) and the maximum normalized iron content (Fe).

freeze-dried samples. Low-field magnetic susceptibility (χ) was measured using an AGICO KLY-2 Kappabridge with an operating frequency of 875 Hz in an applied field of 300 A m^{-1}. ARM was imparted (at the same steps the NRM was demagnetized) along the *z*-axis of the cubic sample with a maximum AF of 120 mT and a DC bias field of 0.1 mT. The anhysteretic susceptibility (χ_{ARM}) was calculated and is defined as the ARM intensity normalized by the static field amplitude, here 0.1 mT. The isothermal remanent magnetization (IRM) was acquired in fields up to 1.2 T using an ASC Scientific Pulse Magnetizer, model IM-10-30, and demagnetized with the cryogenic magnetometer. IRM acquisition was performed in five steps (0, 120, 300, 500, 1200 mT) and for selected samples the IRM was acquired and demagnetized in 20 steps. In addition, the IRM was imparted and measured at liquid nitrogen temperature, that is, the sample was kept at about 77 K.

To complete these rock magnetic measurements, hysteresis properties for 85 samples were recorded using a Princeton MicroMag 2900 alternating gradient magnetometer (AGM). The hysteresis loops were performed in a sweeping mode in fields up to 1 T and an averaging time of 100 ms and the saturation magnetization (M_s), saturation remanence (M_{rs}) and coercivity (B_c) were determined. Subsequently, a remanent magnetization imparted at 1 T was demagnetized in a backfield to obtain the coercivity of remanence (B_{cr}). To test the uniformity of the sample, hysteresis properties were measured on several subsamples. To analyse the coercivity distributions and interaction fields of bulk materials, first order reversal curves (FORCs) were measured on selected samples from unit B, C and E (Pike *et al.* 1999; Roberts *et al.* 2000). These partial hysteresis curves were measured on the AGM by saturating the sample in a 1 T field, decreasing the field down to a determined value, and reversing the field sweep again to saturation. The procedure was repeated following the protocol described by Roberts *et al.* (2000). The FORC diagram was calculated with smoothing factors $SF < 4$ using a MATLAB code by Winklhofer & Zimanyi (2006). The parameters that are responsible for the span and resolution of the FORC were set to $\pm$80 mT for the horizontal axis and 0.5–2 mT for the field increment. These parameters are high enough to identify a central ridge function (Egli *et al.* 2010). This central ridge, a narrow vertical and a broad horizontal distribution of the FORC function was isolated as described by Egli *et al.* (2010). For comparing the FORC diagrams, the switching field distribution of the central ridge, $\rho_{CR}(B_c)$, was normalized by its value at maximum coercivity, ρ_{CR}(max B_c).

In a second step the ESR and FMR spectroscopic properties of 30 samples (about 20 mg) covering the sediment profile were analysed in detail. For units E, C and B the material used for ESR/FMR

spectroscopy and the FORC measurements were collected from the same sample cubes. All spectra were recorded using a X-band Bruker ELEXYS spectrometer, with microwave power of 2 mW, modulation amplitude of 0.1 mT and microwave frequency of 9.87 GHz for room temperature experiments. The spectra were averaged over three sweeps of the applied field from 5 to 600 mT. To compare the FMR signals, the spectral parameters $B_{\rm eff}$, $g_{\rm eff}$, ΔB and A were used, defined as follows. The effective resonance field $B_{\rm eff}$ is the field at maximum absorption and is inversely proportional to the effective g-factor, $g_{\rm eff}$ (e.g. Weiss *et al.* 2004; Kopp *et al.* 2006; Gehring *et al.* 2011b). The line-width ΔB is determined as the width of the absorption spectrum at half its maximum amplitude. The asymmetry ratio A characterizes the proportion of low-field and high-field absorption, with respect to $B_{\rm eff}$ (Kopp *et al.* 2006). Asymmetry ratios of $\sim$1 are characteristic for equidimensional particles, while $A < 1$ are indicative of positive uniaxial anisotropy. In addition, measurements between 5 K and room temperature were performed to identify the possible presence of superparamagnetic particles and to detect magnetite oxidation. The low temperature analysis includes FMR measurements on the same spectrometer as mentioned above with microwave power of 0.02 mW, modulation amplitude of 0.5 mT, and microwave frequency of 9.47 GHz. All low temperature FMR spectra were obtained after zero field cooling to 5 K. These measurements were complemented by saturation induced remanent magnetization (SIRM) measurements using a Quantum Design Physical Property Measurement System (PPMS) magnetometer. The measurements were performed after cooling the samples in the absence of a field, and for the SIRM a field of 2.5 T was applied at 10 K.

For the analytical treatment of the first derivative of the FMR absorption spectra, three different approaches can be considered. First, the FMR signals can be described by mathematical distribution function (e.g. Kopp *et al.* 2006). In this study the first derivative of a Lorentzian function is used to describe the mathematical distribution

$$L'(B) = -\frac{16(B - B_{\rm eff})\,\Gamma)}{\pi\,[4(B - B_{\rm eff})^2 + \Gamma^2]^2}, \quad (1)$$

where B is the applied magnetic field, $B_{\rm eff}$ is the centre and Γ is specifying the width of the Lorentz function ($\Gamma \propto \Delta B$). According to this equation, the spectral parameters $B_{\rm eff}$, and ΔB are adjusted with respect to the measured values. To obtain the best fit, we minimized the sum of squared residuals, where the residuals are defined as the difference between the measured FMR values and the fitted value of the first derivative of the Lorentzian function. Secondly, spectra obtained from well-defined magnetic populations can additionally be simulated using the method described by Charilaou *et al.* (2011b) that yield quantitative uniaxial ($B_{\rm uni}$) and cubic ($B_{\rm cub}$) anisotropy fields. The cubic anisotropy field is determined by the magnetocrystalline field as $B_{\rm cub} = K_1/M$, where K_1 is the first-order anisotropy constant and M is the magnetization of the sample and the uniaxial field is defined as $B_{\rm uni} = 4\pi N_{\rm eff} M$, where $N_{\rm eff}$ is the effective demagnetization factor (Charilaou *et al.* 2011b). Thirdly, the empirical spectral separation is used, when the FMR signals, characterized by superposition of different spectra, cannot be directly simulated or fitted (Gehring *et al.* 2011b). In this approach, FMR spectra are decomposed by subtraction of a synthetically generated spectrum for a specific magnetic population (e.g. equidimensional single-domain non-interacting magnetite particles) to obtain a remaining signal with spectral parameters typical for chain configuration (Gehring *et al.* 2011b). Moreover, the simulation of the ESR spectra, the routine by Stoll & Schweiger (2006) was utilized.

The rock magnetic and FMR spectroscopic analyses are used to characterize the key magnetic traits, that is, concentration, composition, grain size and the configuration of magnetic carriers in the sedimentary record. The magnetic analysis is complemented by X-ray fluorescence (XRF) measurements to determine the relative element content of iron (Fe: 10 kV and 700 μA) and zircon (Zr: 30 kV and 1500 μA). The XRF analysis was performed on split cores by scanning the sediment surface in 1 mm resolution with an AVAATECH X-Ray fluorescence core scanner. The concentration obtained as counts per area were normalized by its maximum.

4 RESULTS

4.1 Rock magnetic properties of the sediment record

The subdivision of the sediment record into units A to F, based on sedimentological criteria, is mirrored by a number of magnetic parameters, for example, χ (Fig. 1). Magnetic susceptibility is sensitive to the total content of magnetic minerals and varies by an order of magnitude, with lowest value in unit D (4.27×10^{-8}m^3 kg^{-1}), followed by a trend toward highest value (1.9×10^{-6} m^3 kg^{-1}) within unit C (Fig. 1, Table 1). In contrast to units B, D and F with their relatively constant values, units A, C and E are rather variable as indicated by the standard deviations of χ (Table 1). The $IRM_{1.2\rm T}$ intensity, which detects only magnetic phases that can carry a remanence, shows values in the range between 0.1×10^{-2} and 1.9×10^{-2} Am^2 kg^{-1} (Fig. 1). Both χ and $IRM_{1.2\rm T}$ are characterized by similar trends across the units E to A, which suggest that the remanence carriers dominate throughout the profile. In unit F, χ values are similar to unit E, but the $IRM_{1.2\rm T}$ exhibits the lowest values within the profile. The similar behaviour of the total Fe-content and the $IRM_{1.2\rm T}$, except for the unit B-C boundary, is evidence that the magnetic carriers are iron phases (Fig. 1). Because no considerable sulfate or sulfide mineral phases are reported from Lake Soppensee (Fischer 1996), the remanent magnetization is most likely carried by iron oxides. Unit F is characterized by IRM-ratios <0.8 (Fig. 1) and residual magnetizations of 25–75 per cent after 120 mT

Table 1. Mean χ values and its standard deviation, mean NRM values and its standard deviation, mean ARM values and its standard deviation, range of MDF ($\rm MDF_{NRM} \approx MDF_{ARM}$) of the different units.

Unit	χ (10^{-6} m^3 kg^{-1})	$NRM_{(0\rm mT)}$ (Am^2 kg^{-1})	$ARM_{(0.1\mu\rm T,0mT)}$ (Am^2 kg^{-1})	$\chi/IRM_{1.2\rm T}$ (A m^{-1})	MDF (mT)
A	0.22 ± 0.15	$(4.12 \pm 4.24)\ 10^{-6}$	$(2.11 \pm 0.81)\ 10^{-5}$	$(3.56 \pm 0.73)\ 10^{-4}$	*n.d.*[a]
B	0.59 ± 0.09	$(3.05 \pm 0.88)\ 10^{-5}$	$(1.75 \pm 0.83)\ 10^{-5}$	$(3.63 \pm 0.69)\ 10^{-4}$	36-45
C	1.28 ± 0.24	$(1.41 \pm 0.35)\ 10^{-4}$	$(2.73 \pm 7.44)\ 10^{-4}$	$(2.01 \pm 0.77)\ 10^{-4}$	36-45
D	0.10 ± 0.05	$(3.34 \pm 1.09)\ 10^{-6}$	$(4.13 \pm 7.11)\ 10^{-6}$	$(5.91 \pm 2.25)\ 10^{-4}$	19-25
E	0.78 ± 0.25	$(2.41 \pm 1.15)\ 10^{-5}$	$(2.99 \pm 1.72)\ 10^{-5}$	$(6.24 \pm 2.33)\ 10^{-4}$	28-48
F	0.78 ± 0.07	$(4.59 \pm 1.20)\ 10^{-6}$	$(9.76 \pm 1.78)\ 10^{-5}$	$(1.30 \pm 1.10)\ 10^{-3}$	*n.d.*[a]

[a](de-)Magnetized by 120 mT AF field is less then 50 per cent.

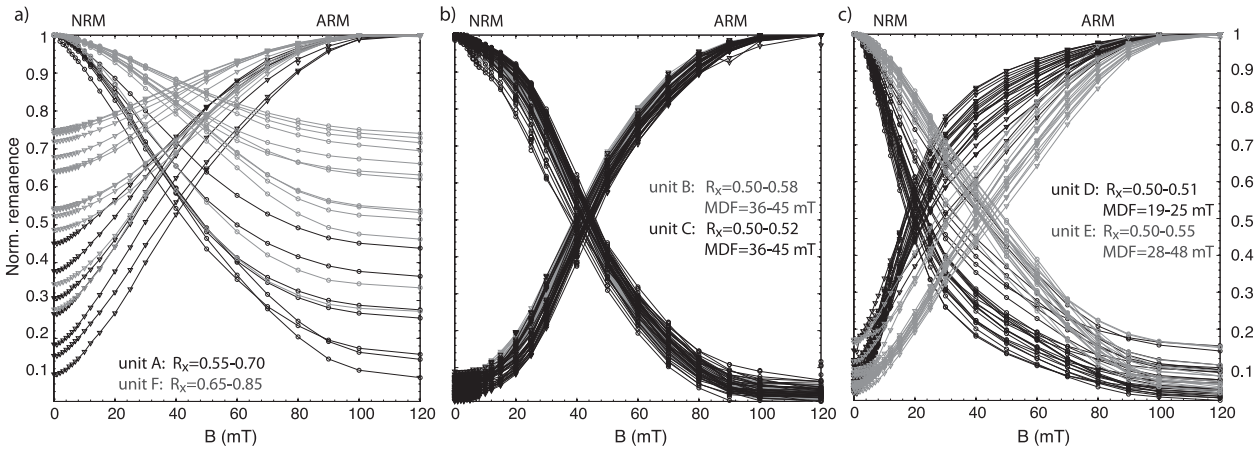

Figure 2. Natural remanent magnetization (NRM) demagnetization and anhysteretic remanent magnetization (ARM) acquisition curves for units A and F (a), units B and C (b), and units D and E (c).

demagnetization of the NRM (Fig. 2a), which indicates that an iron oxide with a relatively high coercivity is the major remanence carrier. The IRM acquired at 77 K is systematically lower than at room temperature IRM ($IRM_{300K}/IRM_{77K} = 1.3 \pm 0.1$). The loss of remanence is presumably due to a Morin transition, therefore the high coercivity phase is interpreted as most likely hematite (Morin 1959; Nagata *et al.* 1961; Özdemir *et al.* 2008). It is worth noting that only in unit F, IRM_{300K}/IRM_{77K} is >1 (units A–E: $IRM_{300K}/IRM_{77K} = 0.8 \pm 0.1$). Eight samples from the uppermost unit A exhibit magnetic properties with low IRM-ratios 0.65–0.80, remaining magnetization between 10 and 45 mT, and magnetization curves with $R_\times > 0.5$ (Fig. 2a). This suggests that the samples contain magnetite/maghemite and a high coercivity phase, such as hematite as magnetic carriers.

The other units exhibit IRM-ratios >0.9, which suggest low-coercive minerals, most likely magnetite or its oxidized counterpart maghemite as the predominant magnetic phase (Fig. 3). Taking the relative Zr content as proxy for detrital input (Blomqvist & Larsson 1994), high Zr contents together with low IRM-ratios in unit F points

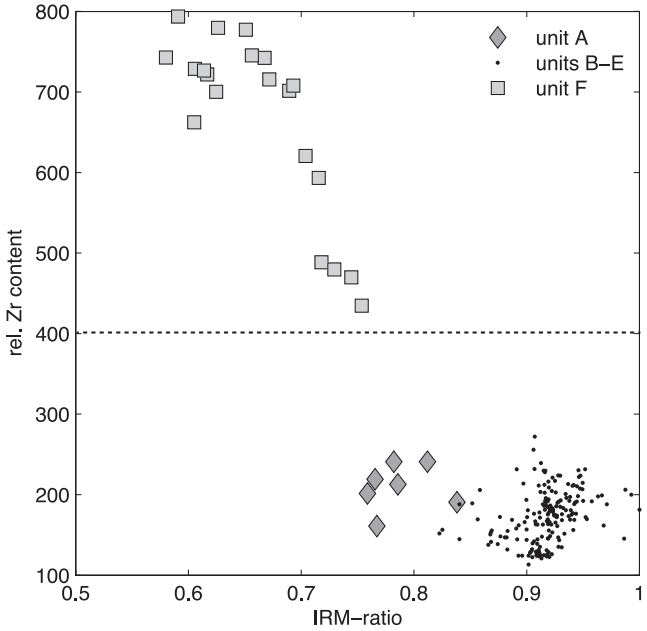

Figure 3. Biplot of relative zircon (Zr) content versus isothermal remanent magnetitation ratio (IRM-ratio = $IRM_{120mT}/IRM_{1.2T}$).

to terrigenous origin of hematite (Fig. 1). The trend of the two variables within the sediment record provides evidence for the vanishing detrital input toward unit E (Figs 1, 3). Therefore, the magnetization of units B-E is caused by authigenic magnetite, whose concentration is the main factor controlling χ, IRM and ARM. There are some moderate variations in concentration-independent parameters such as $ARM_{0.12T}/IRM_{1.2T}$, χ_{ARM}/χ and MDF, which reflects variations in shape, grain size and particle arrangement for authigenic magnetite. The NRM demagnetization and ARM acquisition curves are described by the symmetry with respect to their crossing point $R_\times$, and the MDF. These parameters are used to characterize the magnetite components according to grain size (Dunlop & Özdemir 1997). Even though the NRM and ARM magnetization curves are point-symmetric, the NRM almost completely demagnetized and $R_\times \approx 0.5$, the different units exhibit slight variations in MDF. For samples from unit B, C and D the MDF reveal only little variations between 6 and 9 mT, whereas 20 mT were found for unit E (Fig. 2, Table 1). The magnetization curves of units B, C and D are very similar within each unit, suggesting little variations in the magnetic mineralogy within the units, but clear changes from one unit to the other. It is worth noting that the magnetite population in unit D has a softer magnetization (Table 1). For units B–E the magnetization acquired and demagnetized between 10 and 80 mT indicates magnetite populations in stable single domain state (Moskowitz *et al.* 1993).

Moreover, $ARM_{0.12T}/IRM_{1.2T}$ ratios between 0.1 and 0.2 in units E to B (Fig. 1) are indicative of variations within the single domain properties, such as size and shape (e.g. King *et al.* 1982; Opdyke & Channell 1996; Egli & Lowrie 2002). Further information about grain size variation can be inferred from hysteresis parameters (Table 2), that is, remanence ratio M_{rs}/M_s versus coercivity ratio

Table 2. Mean values of the hysteresis parameters B_c, M_{rs}, squareness (M_{rs}/M_s) and coercivity (B_{cr}/B_c) ratios of the different units.

Unit	M_{rs} ($Am^2\,kg^{-1}$)	M_{rs}/M_s	B_c (mT)	B_{cr}/B_c
A	*n.d.*[a]	*n.d.*[a]	*n.d.*[a]	*n.d.*[a]
B	$8.34\ 10^{-3}$	0.41	23.5	1.63
C	$5.10\ 10^{-2}$	0.4	22.5	1.51
D	*n.d.*[a]	*n.d.*[a]	*n.d.*[a]	*n.d.*[a]
E	$3.83\ 10^{-3}$	0.35	22.7	2.04
F	*n.d.*[a]	*n.d.*[a]	*n.d.*[a]	*n.d.*[a]

[a]Samples are magnetically too weak for recording reproducible hysteresis loops.

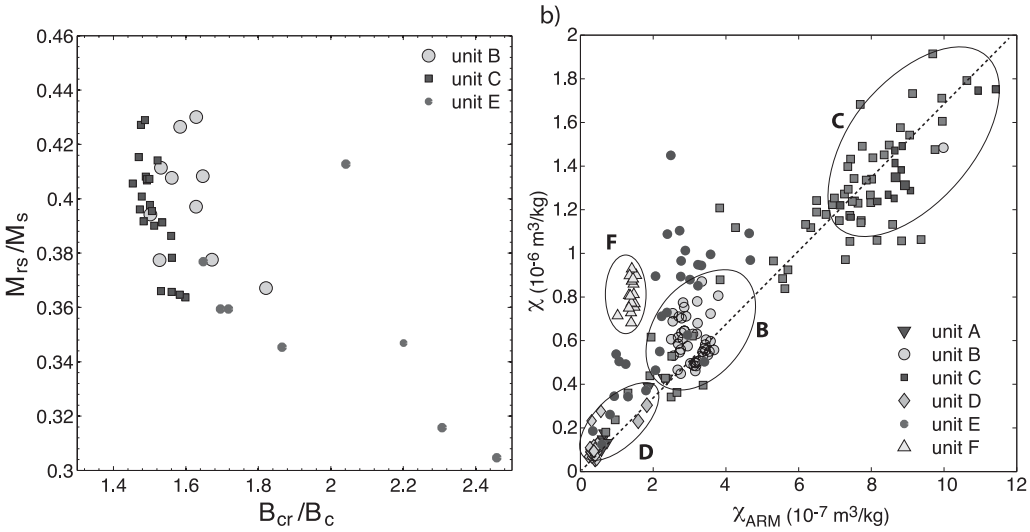

Figure 4. Hysteresis parameters for samples from units B, C and E in the pseudo-single domain range after Day *et al.* (1977) (a) and biplot of χ_{ARM} versus χ for all units (b).

B_{cr}/B_c (Day *et al.* 1977). Unfortunately the weak magnetite response in unit D hampers recording of reproducible hysteresis loops within the experimental error. The same limitation is found for samples from unit F and A, with their low $IRM_{1.2T}$ values. The hysteresis properties displayed in the Day plot confirm the single domain state of magnetite in unit B and C, while unit E exhibit a larger scatter, which indicates less uniform grain size distribution. Additional information about the grain size effects can be gained from the relation of χ_{ARM} to χ (King *et al.* 1982). The scatter of this ratio within unit E is in good agreement with the hysteresis parameters, and the MDF_{NRM} and MDF_{ARM} data. In contrast, samples from unit B, C and D show a linear trend between χ_{ARM} and χ with $\chi_{ARM}/\chi = 0.45 \pm 0.19$ and this has been taken as diagnostic for concentration rather than grain size variations (King *et al.* 1982). By contrast, unit F has χ_{ARM} values distributed parallel to the χ axis (Fig. 4b). The parameter χ indicates the concentration of all magnetic phases in bulk samples, while χ_{ARM} selectively detects single domain particles (Egli & Lowrie 2002). Because of the maximum AF field of 120 mT, χ_{ARM} versus χ reflects grain size variations of low-coercivity minerals. Given this, the response of unit F in the χ_{ARM} versus χ biplot can be explained by high-coercivity phases, but theoretically a superparamagnetic phase, unblocked in the magnetic field during the ARM experiment, cannot be ruled out (Fig. 4b).

Fig. 5 shows for units E, C and B the switching field distributions of the central ridges ($\rho_{CR}(B_c)_{norm}$) and selected FORC diagrams. The switching field distribution extracted from the central ridges of FORC diagrams of unit C shows little variation and a distinct peak at 33 ± 3 mT. Moreover two features can be separated in the FORC diagram; one characterized by a narrow central ridge along $B_b = 0$ mT and the other by relative large vertical spread of $B_b \pm 30$ mT at $B_c = 20$ mT. The latter can be assigned to dispersed interacting magnetite particles, whereas the switching field distribution along of the central ridge can originate either from non-interacting particles with varying aspect ratios or from particles in chain configuration (Egli *et al.* 2010; Kind *et al.* 2011; Roberts *et al.* 2011). The $B_b = 0$ FORC profils of unit B and E are more variable and broader than those from unit C. This suggests higher variation in size and shape of the magnetic carriers. The coercivity peaks for unit E occurs at lower field (B_c around 20 mT) compared to those in unit B (B_c around 20 mT). In both units, however, some samples exhibit similar switching field distributions as those found for unit C and those have been selected for displaying the FORC diagram (Fig. 5).

In summary, the rock magnetic data set obtained from the sediment record provides information about the magnetic mineralogy, in particular the occurrence of detrital, high-coercivity minerals in units A and F and of authigenic single domain magnetite in the other units (Fig. 1). Moreover, magnetic concentration and grain size properties of the magnetite populations as well as evidence for chain configuration have been inferred from magnetic data (Figs 1, 4).

4.2 Spectroscopic properties of the sediment record

All samples from the six units reveal spectral responses from paramagnetic species and from magnetic phases with long-range ordering (Fig. 6). The paramagnetic signal with a six-line pattern, characteristic for Mn(II) with nuclear spin of 5/2 of ^{55}Mn, was found with varying intensities throughout the profile. In unit D and A this signal is most pronounced, but due to temperature dependence of paramagnetic species, the signal can be detected in all units at low temperature (Fig. 7). The Mn(II) signals have a resonance field $B = 352.5$ mT, corresponding to $g = 2.001$ and a hyperfine splitting of 9.4 mT, that is, spacing between spectral lines (Fig. 7). Using the EasySpin software (Stoll & Schweiger 2006) the signal can be simulated with the measured spectral parameters and a zero-field splitting of 8.2 mT, which is characteristic for the Mn(II) structure-bound in calcite (Wildemann 1970). Manganese in its divalent form occurs widespread in natural environments and is indicative of reducing conditions. Considering lacustrine systems, Mn(II) in calcite can either reflect redox conditions in the water column or during diagenesis (Barbaby & Rimstidt 1989; Friedl *et al.* 1997; Müller *et al.* 2006). The ESR data set obtained from the different units permits no unambiguous assignment of redox conditions that could be discussed in an environmental context and therefore, the Mn(II) signals are not further considered. A second rather weak paramagnetic signal occurs at $B = 166$ mT, corresponding to $g = 4.3$ and can be attributed to Fe(III) in a ligand field with orthorhombic distortion, most likely in clay minerals (e.g. Meads & Malden 1975). This signal similar to Mn(II) exhibits an increase in intensity with lowering temperature (Fig. 7).

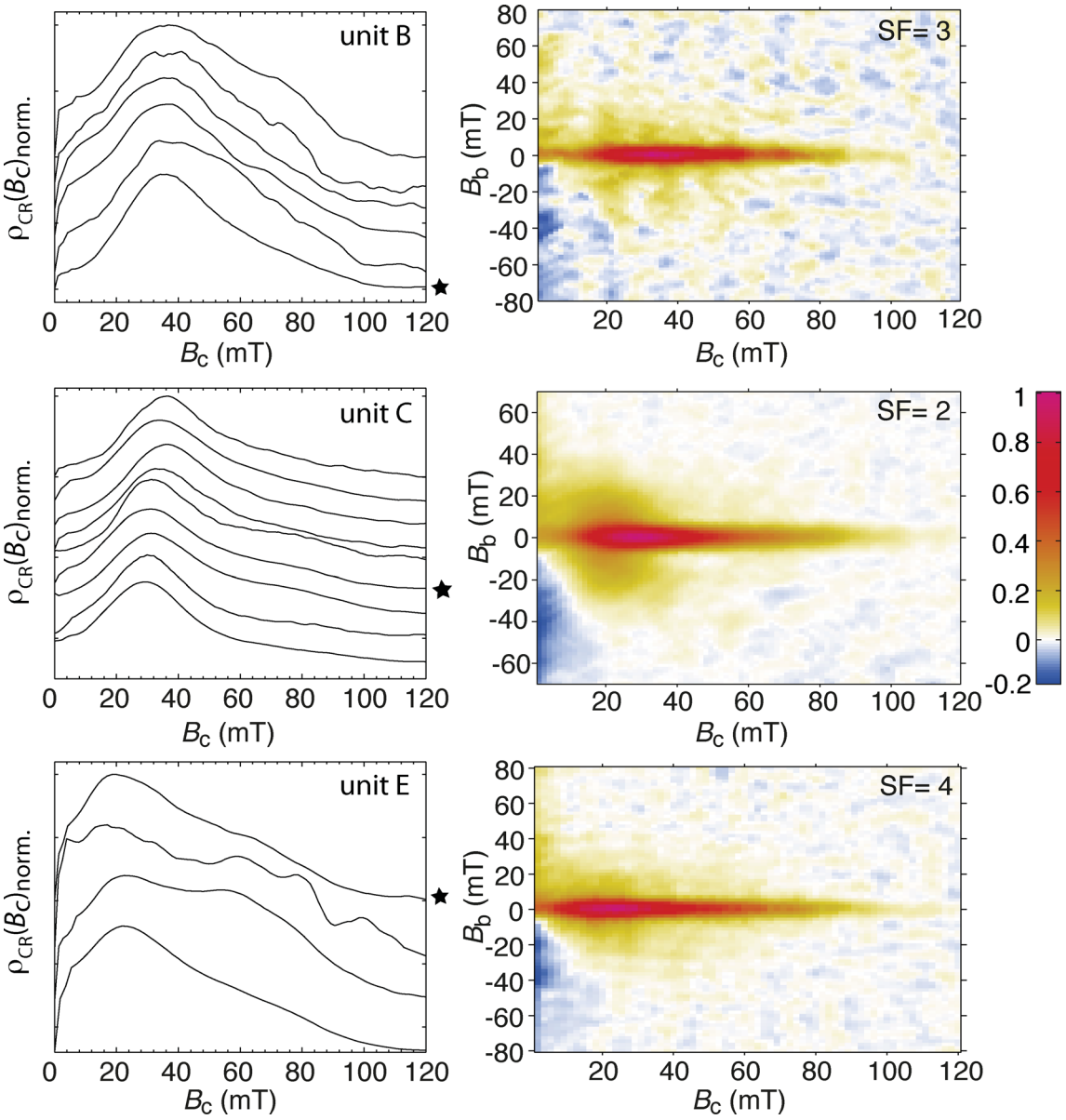

Figure 5. Switching field distributions of the central ridges for samples from units B, C and E and selected FORC diagrams (marked by a star) for each unit. The presented FORC diagrams have resolutions of 3.5 mT (unit B), 1.25 mT (unit C) and 4.5 mT (unit E).

The FMR signals yielded from ferrimagnetic phases dominate the spectra throughout the profile (Fig. 6). By contrast the spectral response of antiferromagnetic phases, such as hematite is limited, because signals arising from canting and/or defect structures are generally weak and broad (Vonsovskii 1966; Gehring & Hofmeister 1994). The FMR spectra from the ferrimagnetic phases vary in their shape and intensity throughout the profile. Because the microwave absorption is proportional to the magnetization of the samples, the variations in intensity correspond to χ and $IRM_{1.2T}$, with highest values in unit C and lowest values found in unit D (Fig. 6). Furthermore, none of the spectra reveals a near zero-field absorption, which suggests the absence of multidomain magnetite (Polder & Smit 1953; Vukadinovic *et al.* 1995; Gehring *et al.* 2009). The spectra within units C, D and F, show only minor variations, and they were further analysed.

Spectra from unit F are characterized by an isotropic signal with $B_{eff} = 351.7 \pm 0.3$ mT and a corresponding $g_{eff} = 2.00$, a narrow line-width $\Delta B = 56.6 \pm 1.1$ mT and an asymmetry ratio $A \approx 1$. Furthermore, a very weak and broad signal was found that is typical for antiferromagnetic phases (e.g. Gehring & Hofmeister 1994). Considering the low IRM-ratios for this unit, the antiferromagnetic phase can be attributed to a high-coercivity mineral, most likely hematite. Because of the extremely weak FMR response of antiferromagnetic phases, a more detailed analysis of the isotropic signal is possible even without spectral separation. All isotropic absorption spectra can be described by a single Lorentzian function and the FMR spectra was fitted with the least squared method using the first derivative of a Lorentzian function (eq. 1). Since the spectra are similar with respect to their parameters g_{eff}, ΔB and A, the fitting is shown for the sample marked with a star in Fig. 6 using $g_{eff} = 2.00$, and $\Delta B = 56.3$ mT (Fig. 7, Table 3). Assuming that the signal originates from one magnetite population, the simulation by Charilaou *et al.* (2011a) leads to anisotropy fields: cubic field $B_{cub} = 15$ mT and uniaxial field $B_{uni} = 0$ mT. A narrow line-width

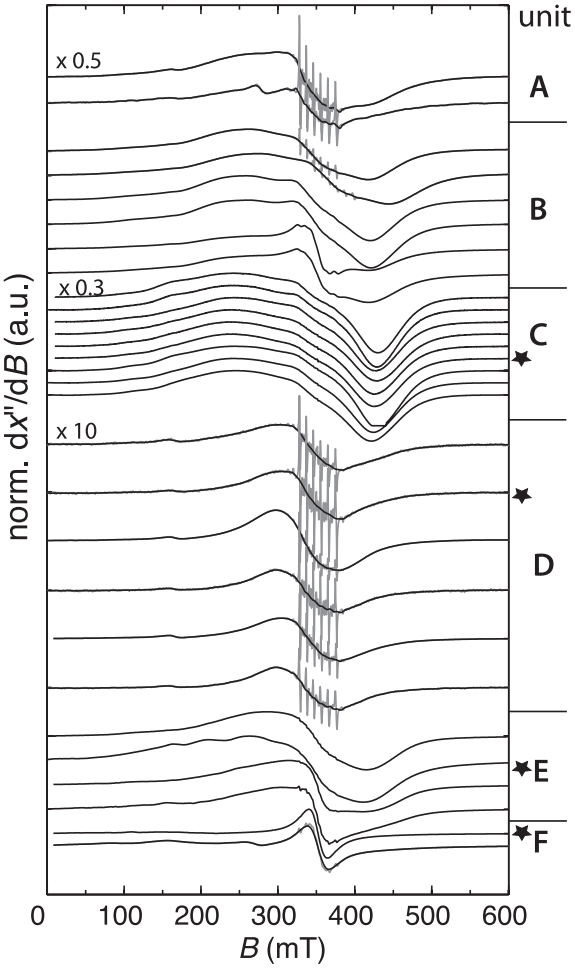

Figure 6. Measured FMR spectra throughout the profile. For comparison reason the signal intensity was adjusted by a gain factor as indicated for unit A (×0.5), unit C (×0.3) and unit D (×10). Samples that are further analysed are marked by a star.

with $g_{\text{eff}} = 2.00$ and $B_{\text{uni}} = 0$ mT point to ferrimagnetic particles in a superparamagnetic state (Sharma & Waldner 1977; Gehring *et al.* 1990; Berger *et al.* 2001; Vargas *et al.* 2008; Charilaou *et al.* 2011a). To confirm the presence of superparamagnetic particles, most likely of magnetite/maghemite in the sediments of unit F, the blocking behaviour was determined (Fig. 7).

The FMR signals between 5 K and room temperature exhibit maximum intensity of the isotropic signal at 80 K. Between 80 and 25 K a slight decrease in intensity is followed by an prominent intensity loss at lower temperatures (Fig. 7a). This loss is accompanied by an increase of ΔB by a factor 2 and a drop of the A-value to 0.6 at $T < 25$ K (Fig. 7b). It is well known that signal broadening is proportional to the increase in anisotropy and a lowering of the asymmetry ratio is indicative of increasing shape anisotropy (Vonsovskii 1966; Kopp *et al.* 2006; Faivre *et al.* 2010). Hence, the anti-correlated behaviour of ΔB and A-value below 25 K can be explained by major blocking of nano-particles. This explanation is in accordance with the low temperature behaviour found for nanoparticles (e.g. Gehring *et al.* 1990; Berger *et al.* 2001; Vargas *et al.* 2008). The remanence behaviour upon heating indicates the superposition of two phases. One is characterized by the distinctive decay up to 23 K, whereas the other has a relatively weak but stable remanence up to room temperature. The latter is assigned to the high-coercivity phase indicated in unit F by the IRM-ratio <0.9. The loss of remanence up to 23 K can be explained by unblocking of superparamagnetic particles in a relative narrow temperature range. It is worth noting that a similar thermal decay of remanence magnetization has been found for siderite with a $T_{\text{N}} \sim 38$ K (Pan & Zhu 2002), but to our knowledge no natural or synthetic Fe carbonate with $T_{\text{N}} \sim 23$ K has been reported in the literature. Given this, the FMR and the remanence data agree well with the interpretation of superparamagnetic magnetite/maghemite particles (Fig. 7).

Samples from unit D exhibit FMR spectra with $g_{\text{eff}} = 2.09 \pm 0.01$, $\Delta B = 122.9 \pm 3.2$ mT and A-values of about 1 (Fig. 8). After removing the Mn(II) signal as proposed by Maloof *et al.* (2007), the absorption spectra can be described as Lorentzian shape. The fitting of the FMR spectra, exemplified for the selected sample marked in Fig. 6 yield $g_{\text{eff}} = 2.08$ and $\Delta B = 120$ mT. Such parameters in concert with the symmetry of the FMR signal shape is indicative of nearly isotropic single domain magnetite with narrow grain size distribution (Fig. 8). These spectral parameters compared to those of the superaramagnetic particles in unit F exhibit similar A-values, but higher g_{eff} and a broadening of ΔB by a factor of 2 (Table 3). The line-width ΔB can be considered as sum of magnetocrystalline anisotropy fields and the internal fields caused by magnetic inhomogeneities (Youssef & Brosseau 2006). In single domain particles, the inhomogeneity field (e.g. demagnetization field) is more pronounced than in superparamagnetic particles, and, therefore, the former exhibit a broadening in ΔB. With this in mind, the A-values of the single domain magnetite provide evidence of nearly equidimensional particles with narrow grain size distribution. This interpretation is consistent to magnetization data with relative low MDF_{NRM} and MDF_{ARM} between 19 and 25 mT (Fig. 2, Table 1).

The FMR spectra obtained from unit C (Fig. 9) exhibit highly asymmetric shapes with two broad shoulders in the low-field absorption range. The mean spectral parameters for this unit are $B_{\text{eff}} = 348.6 \pm 3.0$ mT, which corresponds to $g_{\text{eff}} = 2.02 \pm 0.02$, $\Delta B = 193.2 \pm 3.6$ mT and $A = 0.71 \pm 0.03$. Because the FMR signals cannot be simulated with a single Lorentzian function, a superposition of different magnetic populations is assumed. This is further supported by the decomposition of the ARM and IRM acquisition curves for unit C into two magnetic population that have been reported by Kind *et al.* (2011). To test the assumption of multi-population spectra, an empirical spectral separation was applied (Gehring *et al.* 2011b). It is assumed that the magnetic response originates from two defined populations of magnetic particles. One population consists of single domain magnetite particles with a narrow shape distribution, similar to those found in unit D. Therefore a Lorentzian function with $g_{\text{eff}} = 2.08$, $\Delta B = 120$ mT and $A = 1$ was taken. Subtraction of this spectrum yields the spectral response of the second population with $g_{\text{eff}} = 1.89$ and A-value ≈ 0.5 (Fig. 9). By means of g_{eff}, A-values and the resulting shape of the FMR spectra, the inferred population is characterized by pronounced uniaxial anisotropy. Such anisotropy can be assigned to magnetofossils, where magnetosomes in chain configuration generate an interaction-induced shape anisotropy (Kopp *et al.* 2006; Gehring *et al.* 2011b; Kind *et al.* 2011).

To determine if the magnetofossils are preserved in their original mineralogical form, that is, magnetite, or if they are chemically altered, the temperature dependence of the FMR response was investigated (Gehring *et al.* 2012). Low temperature measurements of the selected sample from unit C exhibit a shift to higher g_{eff} from 2.02 at room temperature to 2.17 at 100 K and to 2.52 at 10 K, which is accompanied by a broadening of ΔB (Fig. 9). Moreover, low temperature signals are less asymmetric and no distinct low-field resonance features can be detected. This can be explained

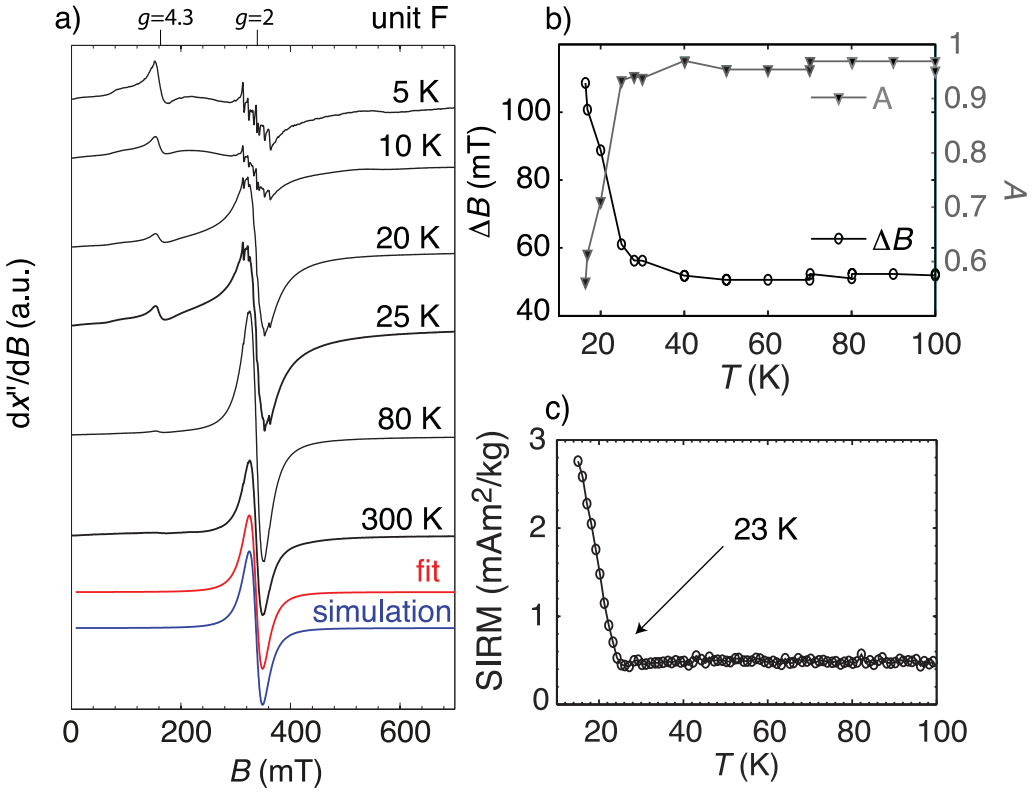

Figure 7. Low temperature FMR series of sample from unit F, marked in Fig. 6, the Lorentzian fit and simulation after Charilaou *et al.* (2011b) of the spectrum at 300 K (a). Spectral parameters asymmetry ratio A and line-width ΔB versus temperature (b) and decay of saturation induced remanence magnetization *SIRM* at 10 K upon heating (c).

Table 3. Mean spectral parameters B_{eff}, g_{eff}, ΔB and A-values and their ranges in parentheses for each unit at room temperature. The number of (sub-) samples: A = 4, B = 7,C = 12, D = 6, E = 5; F = 4.

Unit	B_{eff}	g_{eff}	ΔB	A-value
A	337.2 (332.1–348.6)	2.09 (2.03–2.12)	146.6 (133.2–160.0)	0.76 (0.44–0.95)
B	345.9 (337.4–351.2)	2.04 (2.01–2.09)	170.5 (142.9–178.5)	0.82 (0.79–0.92)
C	348.6 (342.7–351.2)	2.02 (1.99–2.04)	193.2 (184.5–197.8)	0.71 (0.67–0.76)
D	336.6 (335.3–338.5)	2.09 (2.08–2.10)	122.9 (119.9–124.6)	0.98 (0.91–1.04)
E	346.1 (346.2–348.0)	2.03 (2.00–2.09)	155.2 (143.3–186.4)	0.81 (0.66–0.86)
F	351.7 (351.4–352.0)	2.00 (2.00–2.01)	56.6 (55.6–58.1)	0.98 (0.97–1.00)

by the Verwey transition, where the crystal symmetry of magnetite changes from cubic to monoclinic and the easy axis changes from [111] to [100] (e.g. Özdemir *et al.* 1993; Gehring *et al.* 2012). This transition breaks up the preferential alignment of the magnetic moments of the magnetosomes in [111] direction along the chain axis, that is, the uniaxial anisotropy field generated by the interaction induced shape anisotropy diminishes (Gehring *et al.* 2011a). The contribution of the magnetocrystalline anisotropy field to the total anisotropy becomes dominant and the shape anisotropy decreases, which is indicted by the shift to higher g_{eff} values and the vanishing of low-field FMR features (Weiss *et al.* 2004; Gehring *et al.* 2011a). In the case of magnetosomes chains where the Verwey transition is suppressed, the ratio between the contributions of two anisotropy fields are similar within a temperature range between room temperature and 10 K (Gehring *et al.* 2012). Given this it can be argued that the magnetofossils in unit C are preserved as magnetite, that is, in their original mineralogical form. It is worth noting that in a preliminary study, Kind *et al.* (2011) reported oxidized magnetofossils in unit C. Therefore, the preservation of magnetofossils in this unit cannot be considered as uniform.

The FMR spectra within units B and E differ in their shape as indicated by A-values between 0.65 and 0.82, and a line-width between 142 and 186 mT (Fig. 6). The variation in the FMR parameters reveals that magnetite/maghemite particles of these units vary considerably in size and shape. The least uniform spectrum, marked in unit E (Fig. 6) exhibits three features in the low-field absorption range. This sample contains the Laacher See tephra, that is, the spectral superposition is due to *in situ* produced magnetic particles and eolian input of volcanic remains. The application of the empirical spectral separation to isolate magnetic populations with defined magnetic anisotropy properties failed for all samples in unit E and B and this can be explained by complex superposition of spectral responses arising from multiple magnetic populations.

5 DISCUSSION

The subdivision of the sediment record, based on rock magnetic and spectroscopic data is reflected in other environmental proxies, including sedimentological features, stable isotopes and pollen

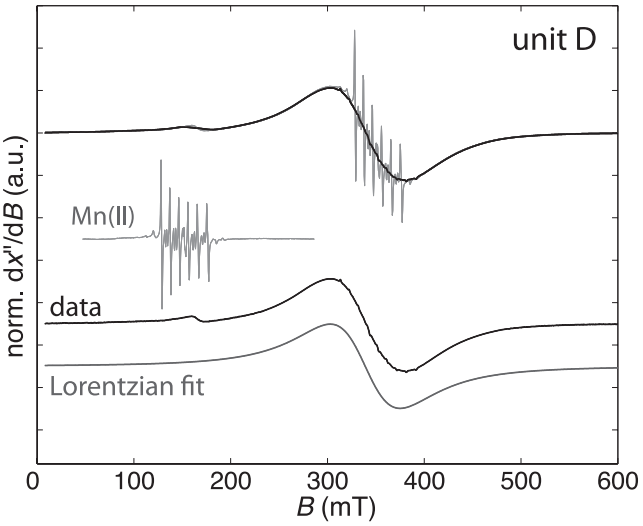

Figure 8. Comparison of the measured spectrum before and after removing the Mn(II) signal of a sample from unit D, marked in Fig. 6 and the Lorentzian fit.

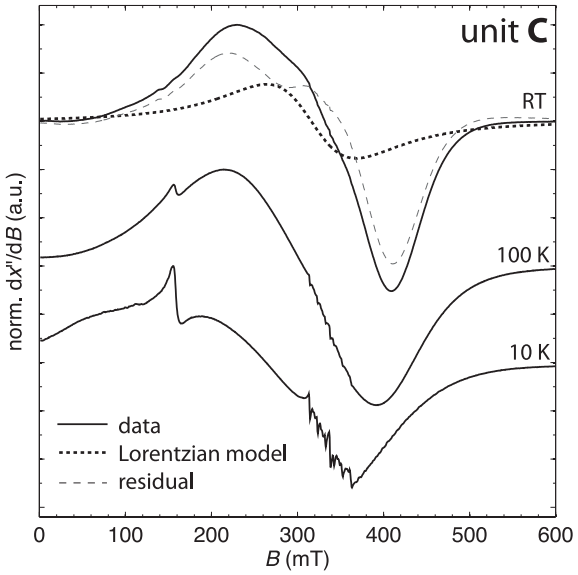

Figure 9. Measured FMR spectra at room temperature, 100 K and 10 K (solid line) of the spectrum from unit C, marked in Fig. 6. The empirical spectral separation, using a Lorentzian fit for dissociated single domain magnetite particles (dotted line) and the residual signal (dashed line) at room temperature.

(e.g. Lotter 1989, 1999, 2001; Hajdas *et al.* 1993; Fischer 1996; Gruber *et al.* 2000; Blockley *et al.* 2008). Therefore, it can be argued that the magnetic response of the sedimentary record is strongly affected by environmental changes. In the following, the FMR and the rock magnetic data of each unit are compared and discussed in an environmental context.

In unit F, the hematite found by rock magnetic methods (IRM-ratio, and NRM demagnetization) is hardly detectable in FMR spectra. In contrast, the occurrence of superparamagnetic magnetite/maghemite particles at room temperature and their blocking behaviour was only detected by FMR spectroscopy. In an environmental context, the stability of detrital hematite suggests prevailing oxic conditions, whereas nano-sized magnetite particles or their oxidized alteration product maghemite is indicative for primary reducing microenvironments. The superparamagnetic particles were probably precipitated in interstitial voids of glacio-lacustrine clays under redox conditions influenced by microbial metabolism. Such microenvironments can be interpreted as starting point to predominant reducing conditions in the depositional environment of Lake Soppensee established at the end of the deglaciation period.

Unit E shows no abundance of detrital high-coercivity minerals, as indicated by the high IRM-ratios. Moreover, the relatively high $ARM_{0.12T}/IRM_{1.2T}$ ratios and the absence of near-zero field absorption in the FMR spectra suggest single domain magnetite or its oxidized counterpart maghemite as the predominant magnetic remanence carrier. It has been shown that the magnetic properties of this magnetic carriers are heterogeneous with respect to their grain size and/or shape, as indicated by the variation of the FORC diagrams and by the χ_{ARM} versus χ biplot for example. The g_{eff}-values, ΔB, A-values and the shape of the FMR spectra reveals similar variations. The heterogeneity is not very surprising, because unit E represents the interstadial Bølling/Allerød, and the stadial Younger Dryas period with its changing climate conditions that can critically affect chemical and biological processes, leading to the precipitation of magnetite in the depositional environment.

Unit D contains calcite varves, which are indicative of stable sedimentological and chemical conditions in the depositional environment, and this agrees well with the formation of single domain magnetite. The FMR spectra show that these particles posses no markedly uniaxial anisotropy. Furthermore, the magnetite particles are dispersed based on the large $\chi_{ARM}/IRM_{1.2T}$ values (Fig. 1). Such equidimensional magnetite particles that are completely isolated from each other can be formed by inorganic precipitation (Maher & Taylor 1988) or by MTB, where the chains collapsed (Kobayashi *et al.* 2006). Therefore, the assignment of these particles to MTB is ambiguous.

Sediments from unit C, however, reveal considerably higher magnetite content as indicated by χ, although the relative Fe concentration changes little (Fig. 1). This hints to a selective accumulation process most likely due to MTB in unit C. Magnetite in configurations of dispersed and chain-arranged particles detected by empirical spectral separation supports the occurrence of MTB and is thus in good agreement with the FORC data. Given this, the required characteristics for biologically controlled magnetite formation, that is, single domain state and chain configuration are fulfilled in unit C. Nevertheless, the question arises, when the colonization of MTB started in Lake Soppensee? Considering the sedimentary record, the predominance of hematite and the absence of stable single domain magnetite in unit F suggest that the appearance of MTB either started in unit E or afterwards. Recently, Paasche & Løvlie (2011), inferred the colonization of MTB in lacustrine systems from remanence parameters, that is, $ARM/IRM_{1.2T} > 0.1$. Applying this approach the colonization of MTB in our record would start in unit E. This parameter in concert with the crossover point $R_{\times}$ of about 0.5 is diagnostic for stable single domain magnetite with relatively narrow size distribution (Moskowitz *et al.* 1993; Snowball 1994). As mentioned earlier such single domain magnetite particles, however, can also be formed by inorganic precipitation (Maher & Taylor 1988). Even though the grain size distribution is among other criteria crucial to detect MTB (Jimenez-Lopez *et al.* 2010), the configuration of the particles is the explicit criterion because chain arrangements in natural system are exclusively generated by MTB (e.g. Philipse & Maas 2002; Kind *et al.* 2011). Unit E provides no clear evidence for MTB or magnetofossils, because first the empirical spectral separation failed to isolate signals with uniaxial characteristics, indicative of magnetite particles in chains or chain-like configuration. This

can be interpreted that either no chains were formed or preserved in the sediments or that the spectral superposition hampers the isolation of a signal arising from interaction-induced shape anisotropy. Secondly, only one FORC digram of unit E permits the isolation of a central ridge (Fig. 5), which can either arise from dispersed magnetic particles with varying aspect ratios or from chain configurations. In summary, with respect to the detection of MTB in unit E both FORC and FMR data remain ambiguous.

NRM and ARM magnetization curves, as well as χ_{ARM}/χ and FORC diagrams, are similar in units B and C. However, most samples in unit B show FMR spectra that are incompatible with intact magnetosome chains typical for MTB. The drop of magnetite concentration and the simultaneous jump in relative Fe concentration in unit B point to a drastic change of the chemical and microbial regime that derogates the preservation of MTB. This change is probably affected by human activity (e.g. forest clearance) at around 2000 yr cal BP, which led to considerable changes in the runoff regime, the erosion dynamics and the beginning of eutrophication, which dominates also unit A (Lotter 1991). There are no rock magnetic or spectroscopic fingerprints for changing conditions in the depositional environments that can be exclusively assigned to eutrophication.

6 CONCLUSION

The study of the sediments from Lake Soppensee demonstrates the potential of FMR spectroscopy in environmental magnetism in two respects. First, FMR analysis supports the rock magnetic data with respect to concentration and grain size of the magnetic particles. Variations in concentration detected by χ and $IRM_{1.2T}$ is seen in the FMR signal intensity, which is proportional to the magnetization of the sample. Further the spectral parameters and the shape of the FMR signals provide an insight into the domain state of low-coercivity phases and their qualitative grain size variations even in samples where the magnetization is too low to record reliable hysteresis loops. Secondly, FMR analysis can complete rock magnetic data. The example from Lake Soppensee shows that MTB can be described by means of anisotropy traits of magnetosomes in chain configuration and therefore, their presence is clearly documented in unit C. In addition, FMR detects superparamagnetic particles at room temperature and their blocking behaviour during cooling experiments. This kind of information was used in our study to infer reducing microenvironment within prevailing oxic depositional environment. Although FMR spectroscopy is a rapid and a non-invasive method to gather experimentally magnetic data, the detailed spectral analysis is a prerequisite to exploit the potential of this method in environmental studies. FMR spectroscopy as well as rock magnetic methods have the same limitations, if natural samples are complex mixtures of magnetic phases. Finally, the application of experimental and analytical FMR spectroscopy in the presented study critically highlights the potential of this method to provide essential information beneficial for future progress in environmental magnetism.

ACKNOWLEDGMENTS

We thank William Lowrie and Ann M. Hirt for critical discussion of the manuscript, Michalis Charilaou for providing the SIRM measurements, and three anonymous reviewers for their comments . The research was financially supported by the CHIRP1 project of ETH (CH1-02-08-2).

REFERENCES

Abragram, A. & Bleaney, B., 1970. *Electron and Paramagnetic Resonance of Transition Ions,* Clarendon Press, Oxford.

Barbaby, R.J. & Rimstidt, J.D., 1989. Redox conditions of calcite cementation interpreted from Mn and Fe contents of authigenic calcites, *Geol. soc. Am. Bull.,* **101,** 795–804.

Berger, R., Bissey, J.-C., Kliava, J., Daubric, H. & Estournés, C., 2001. Temperature dependence of superparamagnetic resonance of iron oxide nanoparticles, *J. Magn. Magn. Mater.,* **234,** 535–544.

Bickford, L.R., 1950. Ferromagnetic absorption in magnetite single crystals, *Phys. Rev.,* **78,** 449–457.

Blockley, S., Ramsey, C., Lane, C. & Lotter, A., 2008. Improved age modelling approaches as exemplified by the revised chronology for the Central European varved Lake Soppensee, *Quatern. Sci. Rev.,* **27,** 61–71 (INTegration of Ice-core, Marine and Terrestrial records (INTIMATE): refining the record of the Last Glacial Interglacial Transition).

Blomqvist, S. & Larsson, U., 1994. Detrital bedrock elements as traces of settling resuspended particulate matter in a coastal area of the Baltic Sea, *Limnol. Oceanogr.,* **39,** 880–896.

Butler, R.F., 1992. *Paleomagnetism: Magnetic Domain to Geologic Terranes,* Blackwell Scientific Publications, Boston, MA.

Charilaou, M., Sahu, K.K., Faivre, D., Fischer, A., García-Rubio, I. & Gehring, A.U., 2011a. Evolution of magnetic anisotropy and thermal stability during nanocrystal-chain growth, *Appl. Phys. Lett.,* **99,** 182505, doi:10.1063/1.3658387.

Charilaou, M., Winklhofer, M. & Gehring, A.U., 2011b. Simulation of ferromagnetic resonance spectra of linear chains of magnetite nanocrystals, *J. appl. Phys.,* **109,** 093903–1–6.

Day, R., Fuller, M. & Schmidt, V.A., 1977. Hysteresis properties of titanomagnetites: grain-size and compositional dependence, *Phys. Earth planet. Inter.,* **13,** 260–267.

Dunlop, D. & Özdemir, O., 1997. *Fundamental Frontiers,* Cambridge University Press, Cambridge.

Egli, R., 2004. Characterization of individual rock magnetic components by analysis of remanence curves. 3. Bacterial magnetite and natural processes in lakes, *Phys. Chem. Earth,* **29,** 869–884.

Egli, R. & Lowrie, W., 2002. Anhysteretic remanent magnetization of fine magnetic particles, *J. geophys. Res.,* **107**(B10), doi:10.1029/2001JB000671.

Egli, R., Chen, A., Winklhofer, M., Kodama, K.P. & Horng, C.-S., 2010. Detection of non-interacting single domain particles using first-order reversal curve (FORC) diagrams, *Geochem. Geophys. Geosys.,* **11,** Q01Z11, doi:10.1029/2009GC002916.

Evans, M.E. & Heller, F., 2003. *Environmental Magnetism Principles and Applications of Enviromagnetics,* Academic Press, New York, NY.

Faivre, D., Fischer, A., García-Rubio, I., Masrogiacomo, G. & Gehring, A.U., 2010. Development of cellular magnetic dipoles in magnetotactic bacteria, *Biophys. J.,* **99,** 1268–1273.

Fischer, A., 1996. Isotopengeochemische Untersuchungen ($\delta^{18}O$ und $\delta^{13}C$) im Wasser und in den Sedimenten des Soppensees (Kt. Luzern, Schweiz), *PhD thesis*, Eidgenössische Technische Hochschule, Zurich.

Fischer, H., Luster, J. & Gehring, A.U., 2007. EPR evidence for maghemitization of magnetite in a tropical soil, *Geophys. J. Int.,* **169,** 909–916.

Fischer, H., Mastrogiacomo, G., Löffler, J.F., Warthmann, R.J., Weidler, P.G. & Gehring, A.U., 2008. Ferromagnetic resonance and magnetic characteristics of intact magnetosome chains in *Magnetospirillum gryphiswaldense, Earth planet. Sci. Lett.,* **270,** 200–208.

Friedl, G., Wehrli, B. & Manceau, A., 1997. Solid phases in the cycling of manganese in eutrophic lakes: new insights from EXAFS spectroscopy, *Geochim. Cosmochim. Acta,* **61,** 275–290.

Gehring, A.U. & Hofmeister, A.M., 1994. The transformation of lepidocriocite during heating: a magnetic and spectroscopic study, *Clays Clay Miner.,* **42,** 409–415.

Gehring, A.U., Karthein, R. & Reller, A., 1990. Activated state in the lepidocrocite structure during thermal treatment, *Naturwissenschaften,* **77,** 177–179.

Gehring, A.U., Fry, I.V., Luster, J. & Sposito, G., 1994. Vanadium in sepiolite: a redox-indicator for an ancient closed brine System in the Madrid Basin, central Spain, *Geochim. Cosmochim. Acta,* **58,** 3345–3351.

Gehring, A.U., Fischer, H., Louvel, M., Kunze, K. & Weidler, P.G., 2009. High temperature stability of natural maghemite: a magnetic and spectroscopic study, *Geophys. J. Int.,* **179,** 1361–1371.

Gehring, A.U., Fischer, H., Charilaou, M. & García-Rubio, I., 2011a. Magnetic anisotropy and Verwey transition of magnetosome chains in Magnetospirillum gryphiswaldense, *Geophys. J. Int.,* **187,** 1215–1221.

Gehring, A.U., Kind, J., Charilaou, M. & García-Rubio, I., 2011b. The detection of magnetotactic bacteria and magnetofossils by means of magnetic anisotropy, *Earth planet. Sci. Lett.,* **309,** 113–117.

Gehring, A.U., Charilaou, M. & García-Rubio, I., 2012. Oxidized magnetosomes in magnetotactic bacteria, *J. Magn. Magn. Mater.,* **324,** 1281–1284.

Gruber, N., Wehrli, B. & Wüest, A., 2000. The role of biogeochemical cycling for the formation and preservation of varved sediments in Soppensee (Switzerland), *J. Paleolimnol.,* **24,** 277–291.

Hajdas, I. & Michczynski, A., 2010. Age-depth model of lake Soppensee (Switzerland) based on the high-resolution ^{14}C chronology compared with varve chronology, *Radiocarbon,* **52,** 1027–1040.

Hajdas, I., Ivy, S.D., Beer, J., Bonani, G., Imboden, D., Lotter, A.F., Sturm, M. & Suter, M., 1993. AMS radiocarbon dating and varve chronology of Lake Soppensee - 6000 to 12000 C-14 years BP, *Clim. Dyn.,* **9,** 107–116.

Hajdas, I., Bonani, G. & Zolitschka, B., 2000. Radiocarbon dating of varve chronologies: Soppensee and Holzmaar lakes after ten years, *Radiocarbon,* **42,** 349–353.

Jimenez-Lopez, C., Romanek, C.S. & Bazylinski, D.A., 2010. Magnetite as a prokaryotic biomarker: a review, *J. geophys. Rev.,* **115,** doi:10.1029/2009JG001152.

Kind, J., Gehring, A.U., Winklhofer, M. & Hirt, A.M., 2011. Combined use of magnetometry and spectroscopy for identifying magnetofossils in sediments, *Geochem. Geophys. Geosyst.,* **12,** Q08008, doi:10.1029/2011GC003633.

King, J., Banerjee, S.K., Marvin, J. & Özdemir, O., 1982. A comparison of different magnetic methods for determining the relative grain size of magnetite in natural materials: some results from lake sediments, *Earth planet. Sci. Lett.,* **59,** 404–419.

Kittel, C., 1948. On the theory of ferromagnetic resonance absorption, *Phys. Rev.,* **73,** 155–161.

Kobayashi, A., Kirschvink, J.L., Nash, C.Z., Kopp, R.E., Sauer, D.A., Bertani, L.E., Voorhout, W.F. & Taguchi, T., 2006. Experimental observation of magnetosome chain collapse in magnetotactic bacteria: sedimentological, paleomagnetic, and evolutionary implications, *Earth planet. Sci. Lett.,* **245,** 538–550.

Kopp, R.E., Nash, C.Z., Kobayashi, A., Weiss, B.P., Bazylinski, D.A. & Kirschvink, J.L., 2006. Ferromagnetic resonance spectroscopy for assessment of magnetic anisotropy and magnetostatic interactions: a case study of mutant magnetotactic bacteria, *J. geophys. Res.,* **111,** B12S25, doi:10.1029/2006JB004529.

Livingstone, D.M. & Hajdas, I., 2001. Climatically relevant periodicities in the thicknesses of biogenic carbonate varves in Soppensee, Switzerland (9740-6870 calendar yr BP), *J. Paleolimnol.,* **25,** 17–24.

Lotter, A.F., 1989. Evidence of annual layering in Holocene sediments of Soppensee, Switzerland, *Aquat. Sci.,* **51,** 19–30, doi:10.1007/BF00877778.

Lotter, A.F., 1991. Absolute dating of the late-glacial period in Switzerland using annually laminated sediments, *Quat. Res.,* **35,** 321–330.

Lotter, A.F., 1999. Late-glacial and Holocene vegetation history and dynamics as shown by pollen and plant macrofossil analyses in anually laminated sediments from Soppensee, central Switzerland, *Veg. Hist. Archaeobot.,* **8,** 165–184.

Lotter, A.F., 2001. The paleolimnology of Soppensee (Central Switzerland), as evidenced by diatoms, pollen, and fossil-pigment analyses, *J. Paleolimnol.,* **25,** 65–79.

Maher, B.A., 2007. Environmental magnetism and climate change, *Contemp. Phys.,* **48,** 247–274.

Maher, B.A. & Taylor, R.M., 1988. Formation of ultrafine-grained magnetite in soils, *Nature,* **336,** 368–370.

Maloof, A.C. *et al.,* 2007. Sedimentary iron cycling and the origin and preservation of magnetization in platform carbonate muds, Andros Island, Bahamas, *Earth planet. Sci. Lett.,* **259,** 581–598.

Mastrogiacomo, G., Fischer, H., Garcia-Rubio, I. & Gehring, A., 2010. Ferromagnetic resonance spectroscopic response of magnetite chains in a biological matrix, *J. Magn. Magn. Mater.,* **322,** 661–663.

Meads, R.E. & Malden, P., 1975. Electron spin resonance in natural kaolinites containing Fe^{3+} and other transition metal ions, *Clay Miner.,* **10,** 313–345.

Morin, F.J., 1959. Oxides which show a metal-to-insulator transition at the neel temperature, *Phys. Rev. Lett.,* **3,** 34–36.

Moskowitz, B., Frankel, R.B. & Bazylinski, D., 1993. Rock magnetic criteria for the detection of biogenic magnetite, *Earth planet. Sci. Lett.,* **120,** 283–300.

Müller, B., Wang, Y. & Wehrli, B., 2006. Cycling of calcite in hard water lakes of different trophic states, *Limnol. Oceanogr.,* **51,** 1678–1688.

Nagata, T., Yama-ai, M. & Akimoto, S., 1961. Memory of initial remanent magnetization and number of repeating of heat treatments in low-temperature behaviour of haematite, *Nature,* **190,** 620–621.

Opdyke, N.D. & Channell, J.E.T., 1996. *Magnetic Stratigraphy,* International Geophysics Series, Academic Press, Burlington, MA.

Özdemir, O., Dunlop, D.J. & Moskowitz, B.M., 1993. The effect of oxidation on the Verwey transition, *Geophys. Res. Lett.,* **20,** 1671–1674.

Özdemir, O., Dunlop, D.J. & Berquó, T.S., 2008. Morin transition in hematite: size dependence and thermal hysteresis, *Geochem. Geophys. Geosyst.,* **9,** doi:10.1029/2008GC002110.

Paasche, Ø. & Løvlie, R., 2011. Synchronized postglacial colonization by magnetotactic bacteria, *Geology,* **39,** 75–78.

Pan, Y. & Zhu, R., 2002. Low-temperature magnetic behavior related to thermal alteration of siderite, *Geophys. Res. Lett.,* **29,** 2087, doi:10.1029/2002GL016021.

Pawse, A., Beske-Diehl, S. & Marshall, S.A., 1998. Use of magnetic hysteresis properties and electron spin resonance spectroscopy for the identification of volcanic ash: a preliminary study, *Geophys. J. Int.,* **132,** 712–720.

Philipse, A.P. & Maas, D., 2002. Magnetic colloids from magnetotactic bacteria: chain formation and colloidal stability, *Langmuir,* **18,** 9977–9984.

Pike, C.R., Roberts, A.P. & Verosub, K.L., 1999. Characterizing interactions in fine magnetic particle systems using first order reversal curves, *J. appl. Phys.,* **85,** 6660–6667.

Polder, D. & Smit, J., 1953. Resonance phenomena in ferrites, *Rev. Mod. Phys.,* **25**(1), 89–90.

Ramsey, C.B., 2008. Deposition models for chronological records, *Quat. Sci. Rev.,* **27,** 42–60.

Roberts, A.P., Pike, C.R. & Verosub, K.L., 2000. First-order reversal curve diagrams: a new tool for characterizing the magnetic properties of natural samples, *J. geophys. Res.,* **105,** 28 461–28 475.

Roberts, A.P. *et al.*, 2011. Magnetotactic bacterial abundance in pelagic marine environments is limited by organic carbon flux and availability of dissolved iron, *Earth planet. Sci. Lett.,* **310,** 441–452.

Schlüchter, C., 1988. The deglaciation of the Swiss-Alps: a paleoclimatic event with chronological problems, *Bulletin de l'Association francaise pour l'etude du quaternaire,* **25,** 141–145.

Sharma, V.K. & Waldner, F., 1977. Superparamagnetic and ferrimagnetic resonance of ultrafine Fe_3O_4 particles in ferrofluids, *J. appl. Phys.,* **48,** 4298–4302.

Snowball, I.F., 1994. Bacterial magnetite and the magnetic properties of sediments in a Swedish lake, *Earth planet. Sci. Lett.,* **126,** 129–142.

Stoll, S. & Schweiger, A., 2006. EasySpin, a comprehensive software package for spectral simulation and analysis in EPR, *J. Magn. Reson.,* **178**(1), 42–55.

Thompson, R. & Oldfield, F., 1986. *Environmental Magnetism,* George Allen & Unwin, London.

Thompson, R., Battarbee, R.W., O'Sullivan, P.E. & Oldfield, F., 1975. Magnetic susceptibility of lake sediments, *Limnol. Oceanogr.,* **20,** 687–698.

Thompson, R., Stober, J.C., Turner, G.M., Oldfield, F., Bloemendal, J., Dearing, J.A. & Rummery, T.A., 1980. Environmental applications of magnetic measurements, *Science,* **207,** 481–486.

Valstyn, E.P., Hanton, J. & Morrish, A., 1962. Ferromagnetic resonance of single-domain particles, *Phys. Rev.,* **128,** 2078–2087.

Vargas, J., Jr, E.L., Zysler, R., Duque, J., Biasi, E.D. & Knobel, M., 2008. Effective anisotropy field variation of magnetite nanoparticles with size reduction, *Eur. Phys. J. B,* **64,** 211–218.

Verosub, K.L. & Roberts, A.P., 1995. Environmental magnetism: past, present, and future, *J. geophys. Res.,* **100,** 2175–2192.

Vonsovskii, S.V., 1966. *Ferromagnetic Resonance: The Phenomenon of Resonant Absorption of a High-Frequency Magnetic Field in Ferromagnetic Substances,* Pergamon Press, Oxford.

Vukadinovic, N., Youssef, Y.B. & Gall, H.L., 1995. Influence of magnetic parameters on microwave absorption of domain mode ferromagnetic resonance, *J. Magn. Magn. Mater.,* **150,** 213–222.

Weiss, B.P., Kim, S.S., Kirschvink, J.L., Kopp, R.E., Sankaran, M., Kobayashi, A. & Komeilia, A., 2004. Ferromagnetic resonance and low-temperature magnetic tests for biogenic magnetite, *Earth planet. Sci. Lett.,* **224,** 73–89.

Wildemann, T.R., 1970. The distribution of Mn^{2+} in some carbonates by electron paramagnetic resonance, *Chem. Geol.,* **5,** 167–177.

Winklhofer, M. & Zimanyi, G.T., 2006. Extracting the intrinsic switching field distribution in perpendicular media: a comparative analysis, *J. appl. Phys.,* **99,** 08E710, doi:10.1063/1.2176598.

Youssef, J.B. & Brosseau, C., 2006. Magnetization damping in two-component metal oxide micropowder and nanopowder compacts by broadband ferromagnetic resonance measurements, *Phys. Rev.,* **74,** 1–13.